RESEARCH ARTICLE

NANO · MICRO small
www.small-journal.com

Controlling Etch Anisotropy of Crystalline Germanium Nanostructures

*Khakimjon Saidov, Zainul Aabdin, Hongwei Yan, Antoine Pacco, Frank Holsteyns, and Utkur Mirsaidov**

Orientation-dependent wet chemical etching of crystalline germanium (c-Ge) is essential for the fabrication of next-generation complementary metal oxide semiconductor (CMOS) devices. Here, using a combination of conventional and in situ liquid-phase transmission electron microscopy (TEM) imaging, we reveal the details of the wet etching process of c-Ge nanostructures and identify critical parameters that control the etching rates along different crystalline directions. We demonstrate that etching behavior can be changed from isotropic to anisotropic etching (i.e., from crystal-orientation-independent to orientation-dependent etching) by introducing hydrochloric acid (HCl) into a commonly used hydrogen peroxide (H_2O_2) etchant. The observations reveal that the relative etching rates along different crystal directions can be tuned by adjusting the HCl concentration, allowing for full control over the etch anisotropy. The study provides important insights into the nanoscale details of the wet etching of c-Ge and presents a new level of control required for the fabrication of advanced nanoelectronic devices.

1. Introduction

The continued demand for energy-efficient and high-performance electronic devices necessitates the development of new nanofabrication methods for a wide range of semiconductor materials.[1–5] Ease of processing, high carrier mobilities, and narrow band gap of Ge and its alloys (e.g., SiGe, GeSn)[6–9] make them attractive materials for transistors,[1,10,11] photodetectors,[8,12,13] and quantum devices.[7] For example, dimensional scaling of future transistors requires precise control over the size and shape of nanostructures that are being fabricated, which can only be achieved by precise nanoscale etching processes where etch selectivity and anisotropy can be accurately controlled.[14–17] Conventional reactive ion etching (RIE) processes lack the selectivity and precision required for producing sub-10-nm devices, as they often result in higher roughness and surface damage comparable to the critical dimensions of the devices, thereby adversely affecting their performance.[1,16] Alternatively, wet chemical etching is not only known to produce damage-free and atomically smooth etch profiles[2,18] but also can be tuned to have significantly higher selectivity than RIE.[1,5] In particular, the highly selective removal of SiGe with respect to Si and SiO_2 by wet etching makes SiGe a popular sacrificial material during the fabrication of advanced transistor architectures.[19,20] Hence, detailed insight into the wet chemical etching of Ge at the nanoscale is essential for devising processes needed for the fabrication of next-generation semiconductor devices.

Ge is typically etched using aqueous oxidizers such as HNO_3 and H_2O_2 solutions because Ge oxides are soluble in water.[21–24] Hence, to explore the nanoscale details of orientation-dependent wet etching of c-Ge in real-time with in situ liquid-phase

K. Saidov, H. Yan, U. Mirsaidov
Department of Physics
National University of Singapore
Singapore 117551, Singapore
E-mail: mirsaidov@nus.edu.sg

K. Saidov, Z. Aabdin, H. Yan, U. Mirsaidov
Center for BioImaging Sciences and Department of Biological Sciences
National University of Singapore
Singapore 117557, Singapore

The ORCID identification number(s) for the author(s) of this article can be found under https://doi.org/10.1002/smll.202504357

DOI: 10.1002/smll.202504357

K. Saidov, U. Mirsaidov
Centre for Advanced 2D Materials and Graphene Research Centre
National University of Singapore
Singapore 117546, Singapore

Z. Aabdin
Institute of Materials Research and Engineering
Agency for Science
Technology and Research (A*STAR)
Singapore 138634, Singapore

A. Pacco, F. Holsteyns
IMEC
Kapeldreef 75, Leuven B-3001, Belgium

U. Mirsaidov
Department of Materials Science and Engineering
National University of Singapore
Singapore 117575, Singapore

TEM, we fabricated liquid cells with c-Ge wagon wheel (WW) nanostructures.[20,25,26] We chose WW geometry because it enables us to accurately probe and compare the etching of multiple crystal facets simultaneously.[27–29] Furthermore, we chose to introduce HCl into the oxidizing etchant solution because HCl is commonly used in surface cleaning in industrial settings and is known to passivate the Ge surfaces.[30–32] We found that by adjusting the HCl concentration in the etchant solution, it is possible to switch from isotropic to anisotropic etching of c-Ge, but it may also be possible to switch the etch anisotropy directions (i.e., select fast and slow etch directions at will) by altering the degree of Cl passivation.

2. Results and Discussion

Figure 1A,B shows the schematic illustration and scanning electron microscopy (SEM) images of the WW platform used for testing the wet chemical etching of epitaxial c-Ge on a Si(100) layer. Here, c-Si base and c-Ge nanospokes are epitaxially grown along the [001] direction as seen from TEM images shown in Figure 1C. The angle between the two sidewalls of each spoke is ≈2.8°, meaning the crystal orientation of both sidewalls is nearly the same. This is important because it ensures that the etching rates at both sidewalls are expected to be the same.

Figure 2 shows the anisotropic etching of c-Ge WWs in an aqueous mixture of 10 mM H_2O_2 and 6 M HCl, where the tips of the spokes along different directions shorten at different rates (Figure 2A,B). The shortening of the spokes is due to the etching of their sidewalls (Figure S2, Supporting Information). For example, ⟨110⟩ spokes are etched significantly faster than the ones along the other crystal directions, with ⟨100⟩ spokes etching the slowest. Notably, the surfaces of all the spokes remain flat with no visible roughening during the etching. The spokes along ⟨110⟩ directions are fully etched within 180 s, leaving only the underlying 30-nm-thick Si layer behind, as seen in the SEM image (Figure 2C); hence, the etching is selective toward Si. Note that the same can be seen in the TEM image series, where the residual faint contrast from the positions of ⟨110⟩ spokes is due to the thin Si layer (Figure 2B: $t = 180$ s). Figure 2D shows a plot of the etching rate for different crystal directions defined as $R = D/t$. Here, D is the sidewall loss after being etched for time duration of t (Figure S2, Supporting Information). The etching rates along different crystal orientations vary between 7 and 17 nm min^{-1} (Figure 2D).

The same etching can also be visualized continuously in real-time using in situ liquid-phase TEM imaging, as shown in **Figure 3**A.[26,36] These observations (Figure 3B,C) are similar to the in-flask observations carried out on a bench and described in Figure 2. Here again, the fastest and slowest etching directions are ⟨110⟩ and ⟨100⟩, respectively, and ⟨320⟩, ⟨520⟩, and ⟨510⟩ directions (i.e., spokes between ⟨110⟩ and ⟨100⟩ directions) etch at intermediate etching rates (Figure 3D,E). It is worth noting here that while the etching in the confinement of the liquid cell may slightly deviate from the etching in bulk solutions, these observations provide a qualitative description of the etching progression, which is in agreement with our in-flask observations.

To investigate how the etch anisotropy of Ge varies with etchant composition, we assessed the etching behaviors in solutions with different H_2O_2 and HCl concentrations (**Figure 4**).

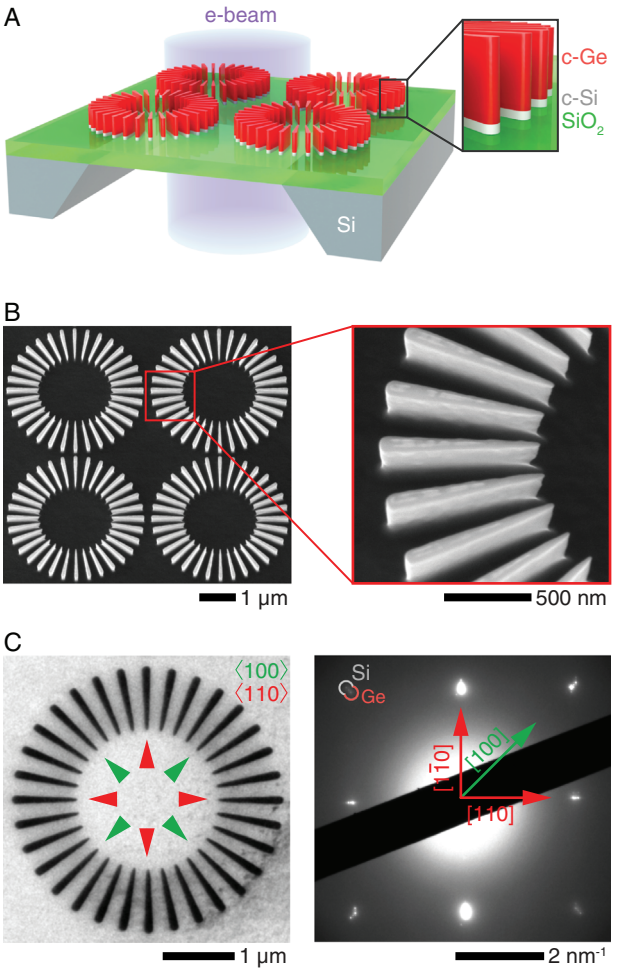

Figure 1. Overview of the Ge wagon wheels (WWs) test platform. A) Schematic and B) SEM images of 4-μm-diameter Ge WW structures fabricated on a silicon-on-insulator (SOI) wafer (Figure S1, Supporting Information). Each spoke comprises a 360-nm-thick c-Ge grown epitaxially on a 30-nm-thick c-Si. The angle between the two sidewalls of each of the thirty-two spokes of a WW is ≈2.8°. C) Top-down TEM image of an individual WW with corresponding selected area electron diffraction image, confirming that c-Si and c-Ge nanospokes are single-crystalline and epitaxially grown along the [001] direction. The red and green arrows in (C) indicate the ⟨110⟩ and ⟨100⟩ directions of Ge (i.e., {110} and {100} are exposed planes), respectively. In the WW, the three spokes between ⟨110⟩ and ⟨100⟩ spokes approximately correspond to ⟨510⟩, ⟨520⟩, and ⟨320⟩ directions. Note that the strain due to 4.2% lattice mismatch at Si/Ge interface produces additional weak spots around the c-Si and c-Ge reflections, as seen in the diffraction image.[33–35]

In pure oxidizer (10 mM H_2O_2), the etching is isotropic, with all crystal directions etching at the rate of $R \approx 7$ nm min^{-1} (Figure 4A,B). However, adding different amounts of HCl into the oxidizer solution induces the etch anisotropy. For example, in a 10 mM H_2O_2 + 6 M HCl solution, the fastest and the slowest etch directions are ⟨110⟩ and ⟨100⟩, respectively. But interestingly, in 15 mM H_2O_2 + 8 M HCl solution, the anisotropy switches, whereby ⟨110⟩ becomes the slowest and ⟨100⟩ the fastest etching directions (Figure 4A,B).

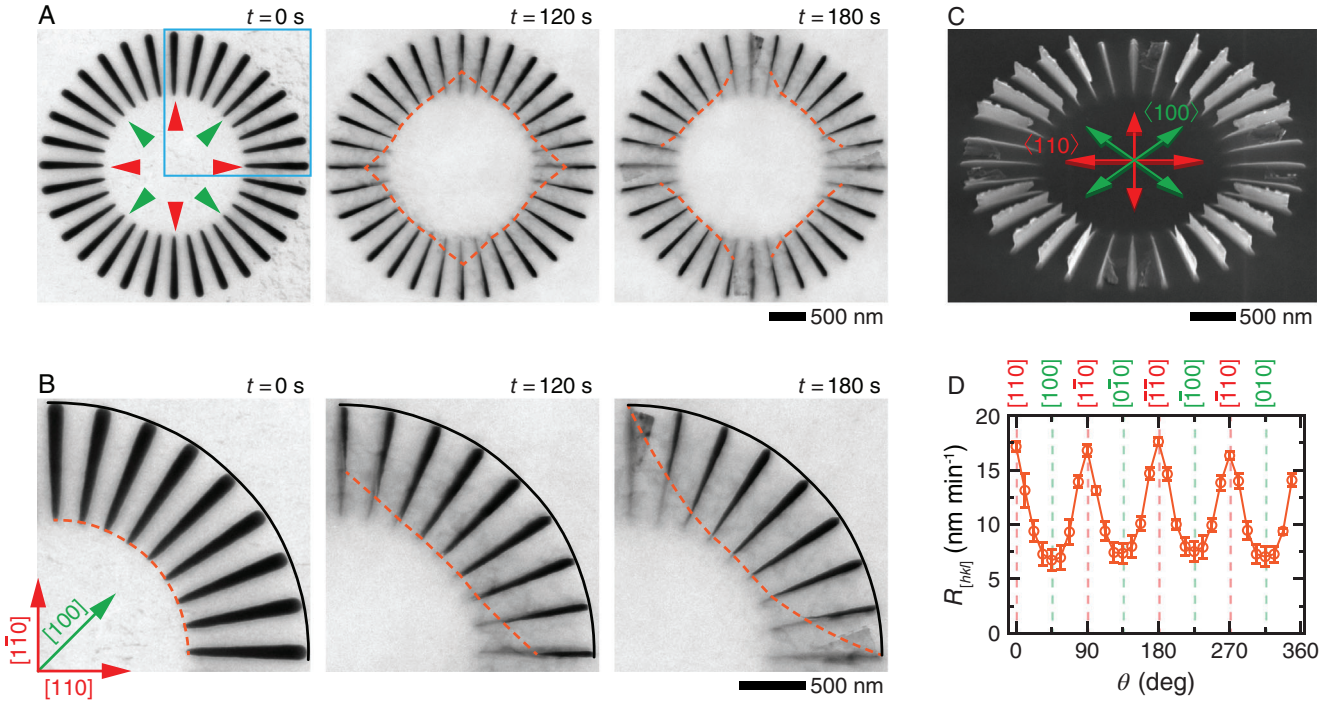

Figure 2. Anisotropic etching of c-Ge WWs. A) A series of TEM images showing the evolution of the c-Ge WWs during in-flask etching in an aqueous solution of 10 mM H_2O_2 + 6 M HCl. B) An enlarged view of the region in panel (A) boxed in blue, showing that different spokes etch at different rates. C) SEM image of a typical Ge WW after etching for 210 s. D) The etching rates of the WW nanospokes as a function of their orientation extracted from t = 120 s image in (A). Here, $\theta = 0°$ corresponds to the [110] direction and increases in the counterclockwise direction. Note that $\theta = 0°$, 11.25°, 22.5°, 33.75°, and 45° correspond to [110], [320], [520], [510], and [100] crystal directions, respectively. The solid black lines in (B) mark the outer edge of the spokes, while the dashed orange lines in (A-B) show how the etch profile evolves with time.

To assess to what extent the anisotropy can be controlled, we tested the etching rates along ⟨110⟩ and ⟨100⟩ directions for a wide range of H_2O_2 and HCl concentrations and evaluated the anisotropic ratio (which we define as $r = \frac{2(R_{\langle 110\rangle} - R_{\langle 100\rangle})}{(R_{\langle 110\rangle} + R_{\langle 100\rangle})}$), as shown in Figure 4C,D. In pure oxidizer solutions (5–20 mM H_2O_2), the (isotropic) etching rate increases with increasing oxidizer concentration (see Figures S3–S5, Supporting Information for additional TEM and SEM images). However, when the etching is anisotropic, which happens when HCl is added to the oxidizer solution, the change in etching rates along different planes is not monotonic and depends on the concentration of H_2O_2 and HCl. For example, when the HCl concentration in a 10 mM H_2O_2 solution was varied from 0 to 10 mM, the etching rate of ⟨110⟩ direction relative to ⟨100⟩ increases for 0 M <[HCl] ≤ 6 M and decreases for 6 M ≤ [HCl] ≤ 10 M (Figure 4C,D). The fast-etching direction switches from ⟨110⟩ to ⟨100⟩ (i.e., $r < 0$) at [HCl] > 8 M. The peak anisotropic ratios for the etchant compositions tested in our study were $r \approx 0.8$ (at [HCl] = 6 M and $[H_2O_2]$ = 10 mM) and $r \approx -0.5$ (at [HCl] = 8 M and $[H_2O_2]$ = 15 mM).

Before discussing the origins of the etch anisotropy, it would be helpful to briefly review the etching of Ge in H_2O_2 solution. When H_2O_2 reacts with Ge surface, it forms water-soluble $Ge(OH)_4$ byproduct ($Ge + 2H_2O_2 \rightarrow Ge(OH)_4$).[24,38,39] Hence, water in an aqueous H_2O_2 solution dissolves the byproducts, leading to isotropic etching (i.e., oxidation of the surface followed by dissolution of $Ge(OH)_4$ on all Ge facets happens at more or less similar rates),[39,40] as confirmed by our observations (Figure 4A,B). Adding HCl into the solution will influence the etching because Cl^- ions bind to Ge dangling bonds and passivate the surface (and hinder the access of H_2O_2 to the surface), reducing the etching rates.[32,41,42] However, the impact on the etching rate will also depend on crystal orientation because the number of dangling bonds is different on different crystal planes. For example, the number of dangling bonds per atom for Ge(110) and (100) surfaces is one and two, respectively, i.e., Ge(100) surface is more reactive than the (110) surface, making (100) planes more susceptible to oxidation.[41,43] These Ge suboxides (Ge^{1+}, Ge^{2+}, Ge^{3+}, and Ge^{4+}) that continuously form on the surface in the presence of H_2O_2 are rather stable (in the absence of HCl) but can be etched away by introducing HCl into the solution.[22,30,42] The complex nature of the interplay between reactants highlights the importance of systematically mapping out the etching behavior as a function of H_2O_2, HCl, and different Ge surfaces, as we have done here (Figure 4C,D).

While it is impossible to pinpoint how these different processes will impact the etching rate in tandem, it is still possible to propose a qualitative description of the process. For illustration purposes, let us examine the changes in etching rates along ⟨110⟩ and ⟨100⟩ directions when [HCl] is varied from 0 to 10 M at a fixed $[H_2O_2]$ = 10 mM. (Figure 4C). At lower to moderate HCl concentrations, in addition to the dissolution in water, $Ge(OH)_4$ is also being etched by Cl^-. Hence, the etching rates along both crystal directions increase with increasing HCl concentration.

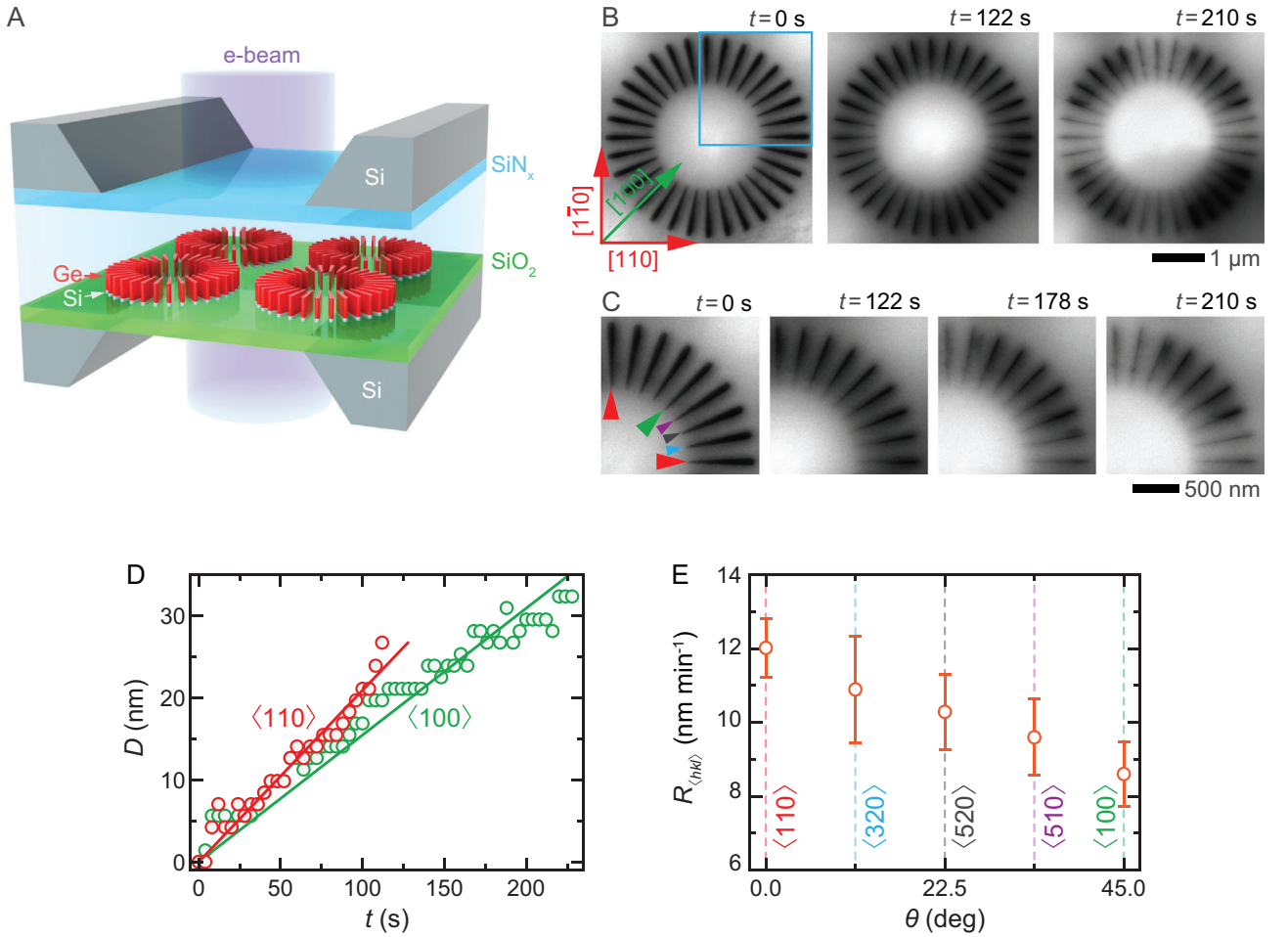

Figure 3. Imaging anisotropic etching of c-Ge WW with in situ liquid cell TEM. A) Schematic of the liquid cell used for real-time in situ TEM imaging, in which the etching solution is encapsulated between two Si chips: top chip with SiN_x window and bottom chip with c-Ge WW patterned onto its SiO_2 window for TEM imaging. B) TEM image series showing the anisotropic etching of c-Ge WWs in an aqueous solution of 10 mM H_2O_2 + 6 M HCl at room temperature (Video S1, Supporting Information). To minimize the impact of the electron beam on the etching process, the image series was acquired with a low electron flux of ≈0.1 e^- Å^{-2} s^{-1}.[37] C) An enlarged view of the region in panel (B) boxed in blue. The spokes at the ⟨110⟩, ⟨320⟩, ⟨520⟩, ⟨510⟩, and ⟨100⟩ directions are indicated with the red, blue, black, purple, and green arrows, respectively. D) Etch depth (D) of the spokes along the ⟨100⟩ and ⟨110⟩ directions as a function of etching time. Red and green lines are the linear fits, with corresponding etching rates of ≈0.2 and ≈0.15 nm s^{-1} along ⟨110⟩ and ⟨100⟩ directions, respectively. (E) Average etching rates of the spokes at different orientation angles, θ, with 0°, 11.25°, 22.5°, 33.75°, and 45° corresponding ⟨110⟩, ⟨320⟩, ⟨520⟩, ⟨510⟩, and ⟨100⟩ crystal directions, respectively.

Because the reactivity between the different planes and Cl^- is different, etching in the presence of HCl results in anisotropic etching. At high HCl concentrations, excess Cl^- ions also start to passivate the freshly etched Ge surface, thereby reducing the etching rates. Again, due to the difference in reactivity, as mentioned earlier, the two etching rates peak at different concentrations; hence, at high HCl concentrations, the etch anisotropy switches (**Figure 5**). While this assessment offers a plausible description of what is causing the switch in etch anisotropy to enable control over the etch directions, future studies focusing on surface chemistry are needed to pinpoint the exact etching mechanism of Ge.

In summary, we show that the etching of c-Ge can be controlled to produce either isotropic or anisotropic etch profiles needed for dimensional scaling and advancing new 3D architectures for the next-generation integrated circuits. Control over the etching directions is achieved simply by introducing HCl into an aqueous oxidizer solution during wet chemical etching. Our approach to directly visualizing the nanoscale etching along multiple crystal orientations is not limited to Ge and can be easily extended to other semiconductors (Figure S6 and Video S2, Supporting Information). Thus, we believe that the presented approach will aid in developing and optimizing new processes for the manufacturing of semiconductor devices.

3. Experimental Section

3.1. Materials

The following chemicals were used to study the etching of WWs: hydrogen peroxide (30% H_2O_2, Dickson Chemical, Singapore), hydrochloric acid (37% HCl, Cat. No. 258 148, Sigma–Aldrich

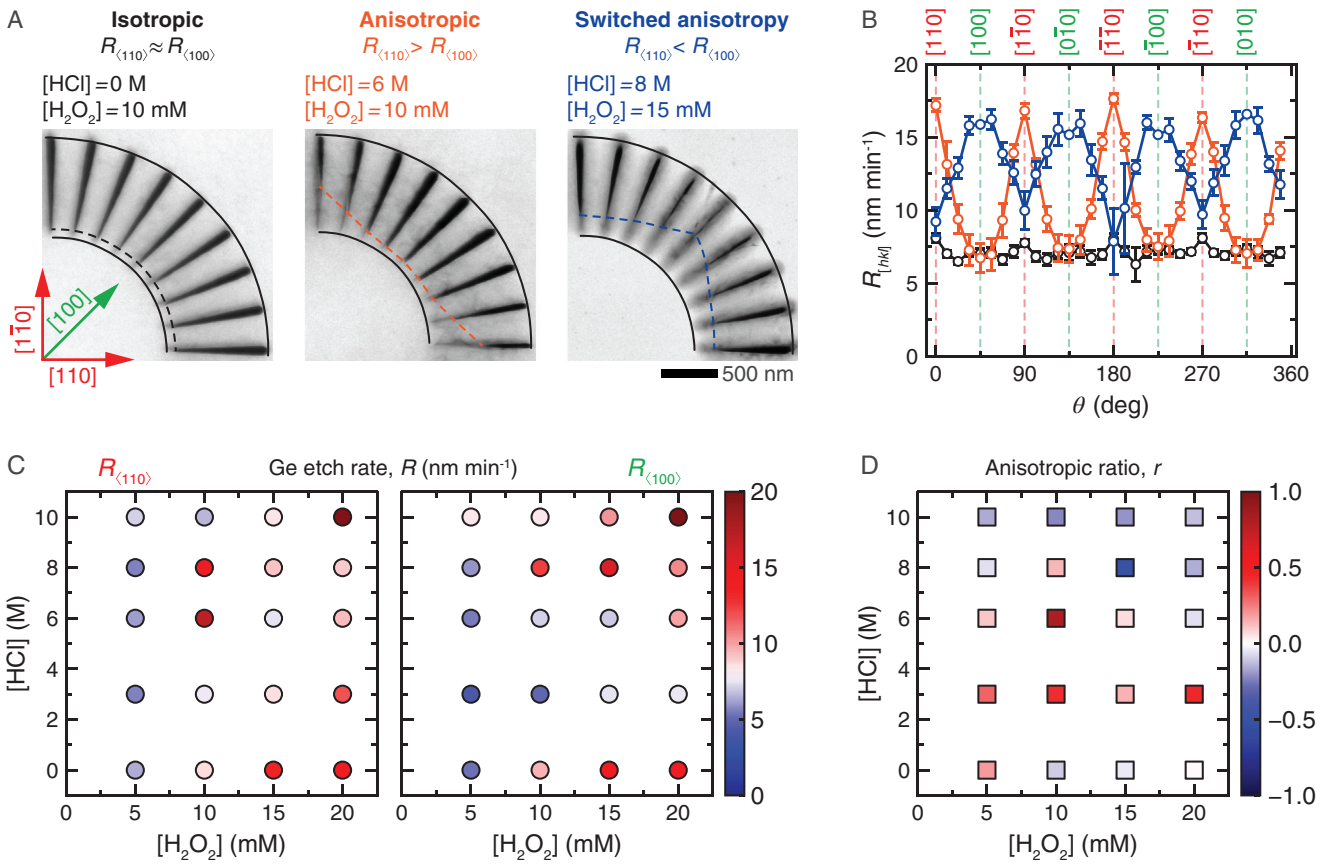

Figure 4. Detailed assessment of the anisotropic etching of c-Ge in H_2O_2 + HCl solution. A) TEM images of Ge WWs after isotropic etching in pure oxidizer solution (10 mM H_2O_2), anisotropic etching in a mixture solution of 10 mM H_2O_2 + 6 M HCl, and 15 mM H_2O_2 + 8 M HCl for t = 120 s. Note that the fast etch directions differ by 90° for the last two solutions. B) The etching rates of the WW nanospokes as a function of their spatial orientation, θ, for the three conditions shown in (A). C) Etching rates along ⟨110⟩ and ⟨100⟩ directions and D) the strength of the etch anisotropy as a function of HCl and H_2O_2 concentrations (see the text for the definition).

Co. LLC, St. Louis, USA), potassium hydroxide (semiconductor grade KOH pellets, Cat. No. 306 568, Sigma–Aldrich Co. LLC, St. Louis, USA), and hydrofluoric acid (48% wt. HF in water, Cat. No. 339 261, Sigma–Aldrich Co. LLC, St. Louis, USA). The aqueous solutions in this study were prepared using deionized (DI) water (ρ_{H_2O} = 18.2 MΩ cm).

3.2. Fabrication of c-Ge Wagon Wheels (WWs)

c-Ge WWs were fabricated on a 300-mm standard p-type (B-doped, 1–100 Ω cm) (100) silicon-on-insulator (SOI) wafer. First, the c-Si device layer was thinned down to 30 nm using chemical mechanical polishing (CMP), and a 360-nm-thick c-Ge layer was grown epitaxially on the device layer. Next, a 50-nm-thick SiN_x film was deposited on both sides of the wafer as a hard mask using the low-pressure chemical vapor deposition (LPCVD) technique. Then, WW patterns were transferred onto the SiN_x film on the device layer side of the wafer using a 193-nm immersion lithography and CF_4/CH_4F_2 plasma etching of the photoresist. With patterned SiN_x serving as a hard mask, exposed c-Ge/c-Si layers were etched by an SF_6 plasma etching in an ambient N_2 atmosphere to create WW structures. Finally, the SiN_x hard mask was removed using a hot phosphoric acid (85 wt.% H_3PO_4 at 160 °C for 6 min). The SEM images of the wafer with the patterned c-Ge WW array are shown in Figure S1 (Supporting Information). To produce chips with WWs on a free-standing SiO_2 window film, the 300-mm wafer was diced into square pieces (72 × 72 mm^2). The chips were fabricated from these square wafer pieces using conventional microfabrication techniques, such as photolithography, deep reactive ion etching (DRIE), and wet etching of bulk Si to release the membrane.[14]

3.3. Fabrication of Liquid Cell Chips

Prior to in situ liquid-phase TEM studies, both the bottom and the top chips were cleaned with air plasma for 2 min. The bottom chips (with WWs) were further cleaned in 0.25% wt. HF for 2 min followed by rinsing in DI water and blow-drying with N_2 gas. Next, a liquid cell comprising a WW-patterned bottom chip and a top chip with a flat SiN_x membrane was assembled and loaded into a custom-built liquid-flow TEM holder for in situ TEM studies.[14,26] The detailed fabrication steps of the top chips and assembling and loading processes were described in our

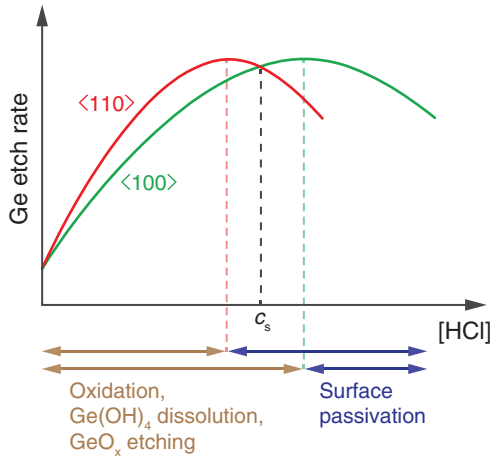

Figure 5. Schematic plot representing the effect of HCl on the etching rate along ⟨110⟩ and ⟨100⟩ directions of c-Ge. Red and green curves represent the etching rates along ⟨110⟩ and ⟨100⟩ directions, respectively. For both ⟨110⟩ and ⟨100⟩ directions, the etching rates increase first and reach their maximum values, followed by a decrease in etching rates as Cl^- passivation of the surface starts to dominate. c_s is the HCl concentration at which the fast etching direction switches from ⟨110⟩ to ⟨100⟩.

earlier studies.[25,26,36] The bottom chips were fabricated from the Si wafer with patterned c-Ge WWs.

3.4. TEM and SEM Imaging

A 200 kV JEOL2010F TEM (JEOL Ltd., Tokyo, Japan) equipped with a Gatan OneView camera (Gatan Inc., Pleasanton, CA, USA) was used for both in-flask and in situ TEM imaging. The in situ etching studies displayed in Figure 3 (Video S1) and Figure S6 (Video S2) (Supporting Information) were conducted with the etchant flow rate in the range of 3–5 µL min^{-1} using a custom flow-cell TEM holder.[15,32] In situ TEM image series from these studies were acquired at a rate of 5 frames per second with low electron flux < 0.1 e $Å^{-2}$ s^{-1}. An FEI Verios 460L field emission scanning electron microscope (FESEM) (Thermo Fisher Scientific Ltd., Hillsboro, OR, USA) was used for SEM imaging.

3.5. Image Processing

The drift correction and image processing codes were written in Python 2.7 using NumPy,[44] SciPy,[45] OpenCV,[46] HyperSpy,[47] and Matplotlib[48] libraries. To improve the contrast of the final images and in situ movies, the image sequence was drift-corrected and averaged every 10 frames.

To measure the etching rates, the locations of the WW and its spokes were detected through template matching using a hollow disk template of the same size as the WWs. The symmetry of individual nanospokes was used to detect the precise location and orientation of each spoke. For each spoke, the etching rate can be measured from the change in the position of its sidewalls (Figure S2, Supporting Information). Next, after identifying the sidewall positions of each spoke at different timepoints, the etching rates were calculated by measuring the moving distances of the sidewall of the spokes (i.e., sidewall-loss) over time. The etching rate of each spoke was then defined as the average of the rates from the two sidewalls of each spoke.

Supporting Information

Supporting Information is available from the Wiley Online Library or from the author.

Acknowledgements

This work was supported by Singapore's National Research Foundation (NRF), under the Competitive Research Program (CRP) funding (NRF-CRP23-2019-0001).

Conflict of Interest

The authors declare no conflict of interest.

Data Availability Statement

The data that support the findings of this study are available from the corresponding author upon reasonable request.

Keywords

etching, germanium, in situ TEM, nanofabrication, semiconductors

Received: April 8, 2025
Revised: July 23, 2025
Published online: August 29, 2025

[1] P. S. Goley, M. K. Hudait, *Materials* **2014**, *7*, 2301.
[2] H. H. Radamson, X. He, Q. Zhang, J. Liu, H. Cui, J. Xiang, Z. Kong, W. Xiong, J. Li, J. Gao, H. Yang, S. Gu, X. Zhao, Y. Du, J. Yu, G. Wang, *Micromachines* **2019**, *10*, 293.
[3] S. Thomas, *Nat. Electron.* **2021**, *4*, 452.
[4] K. J. Kuhn, *IEEE Trans. Electron Devices* **2012**, *59*, 1813.
[5] H. H. Radamson, H. Zhu, Z. Wu, X. He, H. Lin, J. Liu, J. Xiang, Z. Kong, W. Xiong, J. Li, H. Cui, J. Gao, H. Yang, Y. Du, B. Xu, B. Li, X. Zhao, J. Yu, Y. Dong, G. Wang, *Nanomaterials* **2020**, *10*, 1555.
[6] R. Pillarisetty, *Nature* **2011**, *479*, 324.
[7] G. Scappucci, C. Kloeffel, F. A. Zwanenburg, D. Loss, M. Myronov, J.-J. Zhang, S. De Franceschi, G. Katsaros, M. Veldhorst, *Nat. Rev. Mater.* **2021**, *6*, 926.
[8] J. Michel, J. Liu, L. C. Kimerling, *Nat. Photonics* **2010**, *4*, 527.
[9] J. Doherty, S. Biswas, E. Galluccio, C. A. Broderick, A. Garcia-Gil, R. Duffy, E. P. O'Reilly, J. D. Holmes, *Chem. Mater.* **2020**, *32*, 4383.
[10] H. Shang, M. M. Frank, E. P. Gusev, J. O. Chu, S. W. Bedell, K. W. Guarini, M. Ieong, *IBM J. Res. Dev.* **2006**, *50*, 377.
[11] L. Wind, M. Sistani, R. Böckle, J. Smoliner, L. Vukusic, J. Aberl, M. Brehm, P. Schweizer, X. Maeder, J. Michler, F. Fournel, J.-M. Hartmann, W. M. Weber, *Small* **2022**, *18*, 2204178.
[12] L. Colace, G. Masini, F. Galluzzi, G. Assanto, G. Capellini, L. Di Gaspare, F. Evangelisti, *Solid State Phenom.* **1997**, *54*, 55.
[13] Y. Kang, Z. Huang, Y. Saado, J. Campbell, A. Pauchard, J. Bowers, M. J. Paniccia, presented at *High Performance Ge/Si Avalanche Photodiodes Development in Intel. Optical Fiber Communication Conf./National Fiber Optic Engineers Conf. 2011*, Los Angeles, California USA, March **2011**.

[14] Z. Aabdin, T. Ghosh, A. Pacco, S. Raj, H. T. B. Do, K. Saidov, T. W. Weei, U. Anand, P. Král, F. Holsteyns, M. Bosman, U. Mirsaidov, *ACS Appl. Electron. Mater.* **2022**, *4*, 5191.
[15] M. A. Gosálvez, P. Pal, N. Ferrando, K. Sato, *J. Micromech. Microeng.* **2011**, *21*, 125008.
[16] P. Pal, K. Sato, *Micro and Nano Systems Letters* **2015**, *3*, 6.
[17] P. Pal, K. Sato, M. A. Gosalvez, M. Shikida, *J. Micromech. Microeng.* **2007**, *17*, 2299.
[18] M. A. Gosálvez, K. Sato, A. S. Foster, R. M. Nieminen, H. Tanaka, *J. Micromech. Microeng.* **2007**, *17*, S1.
[19] S. Barraud, B. Previtali, V. Lapras, R. Coquand, C. Vizioz, J. M. Hartmann, M. Cassé, *Semicond. Sci. Technol.* **2019**, *34*, 074001.
[20] Z. Baraissov, A. Pacco, S. Koneti, G. Bisht, F. Panciera, F. Holsteyns, U. Mirsaidov, *ACS Appl. Mater. Interfaces* **2019**, *11*, 36839.
[21] S. Kagawa, T. Mikawa, T. Kaneda, *Jpn. J. Appl. Phys.* **1982**, *21*, 1616.
[22] B. L. Ong, S. W. Ong, A. Rusydi, E. S. Tok, *Appl. Surf. Sci.* **2020**, *530*, 147256.
[23] S. Sioncke, D. P. Brunco, M. Meuris, O. Uwamahoro, J. V. Steenbergen, E. Vrancken, M. M. Heyns, *ECS Trans.* **2008**, *16*, 451.
[24] I. M. Huygens, W. P. Gomes, K. Strubbe, *ECS Trans.* **2007**, *6*, 375.
[25] Z. Aabdin, X. M. Xu, S. Sen, U. Anand, P. Král, F. Holsteyns, U. Mirsaidov, *Nano Lett.* **2017**, *17*, 2953.
[26] U. Anand, T. Ghosh, Z. Aabdin, S. Koneti, X. Xu, F. Holsteyns, U. Mirsaidov, *Proc. Natl. Acad. Sci. USA* **2021**, *118*, 2108074118.
[27] R. A. Wind, M. A. Hines, *Surf. Sci.* **2000**, *460*, 21.
[28] A. Pacco, Z. Tao, J. Rip, D. van Dorp, H. Philipsen, F. Holsteyns, *Nanoscale Res. Lett.* **2019**, *14*, 285.
[29] M. A. Gosálvez, P. Pal, N. Ferrando, H. Hida, K. Sato, *J. Micromech. Microeng.* **2011**, *21*, 125007.
[30] T. Hanrath, B. A. Korgel, *J. Am. Chem. Soc.* **2004**, *126*, 15466.
[31] P. Ponath, A. B. Posadas, A. A. Demkov, *Appl. Phys. Rev.* **2017**, *4*, 021308.
[32] S. Sun, Y. Sun, Z. Liu, D.-I. Lee, S. Peterson, P. Pianetta, *Appl. Phys. Lett.* **2006**, *88*, 021903.
[33] S. Roychowdhury, T. Ghosh, R. Arora, M. Samanta, L. Xie, N. K. Singh, A. Soni, J. He, U. V. Waghmare, K. Biswas, *Science* **2021**, *371*, 722.
[34] I.-T. Bae, Z. R. Lingley, B. J. Foran, P. M. Adams, H. Paik, *Sci. Rep.* **2023**, *13*, 19018.
[35] C. Lee, Y.-S. Yoo, B. Ki, M.-H. Jang, S.-H. Lim, H. G. Song, J.-H. Cho, J. Oh, Y.-H. Cho, *Sci. Rep.* **2019**, *9*, 11709.
[36] K. Saidov, I. Erofeev, Z. Aabdin, A. Pacco, H. Philipsen, A. W. Hartanto, Y. Chen, H. Yan, W. W. Tjiu, F. Holsteyns, U. Mirsaidov, *Adv. Funct. Mater.* **2024**, *34*, 2310838.
[37] B. Fritsch, S. Lee, A. Körner, N. M. Schneider, F. M. Ross, A. Hutzler, *Adv. Mater.* **2025**, *37*, 2415728.
[38] D. Schmeisser, R. D. Schnell, A. Bogen, F. J. Himpsel, D. Rieger, G. Landgren, J. F. Morar, *Surf. Sci.* **1986**, *172*, 455.
[39] G. H. A. Abrenica, M. V. Lebedev, M. Fingerle, S. Arnauts, N. Bazzazian, W. Calvet, C. Porret, H. Bender, T. Mayer, S. d. Gendt, D. H. Dorp, *J. Mater. Chem. C* **2020**, *8*, 10060.
[40] G. H. A. Abrenica, M. V. Lebedev, H. Le, A. Hajduk, M. Fingerle, T. Mayer, S. d. Gendt, D. H. Dorpv, *J. Mater. Chem. C* **2019**, *7*, 4846.
[41] P. W. Loscutoff, S. F. Bent, *Annu. Rev. Phys. Chem.* **2006**, *57*, 467.
[42] G. H. A. Abrenica, M. Fingerle, M. V. Lebedev, S. Arnauts, T. Mayer, F. Holsteyns, S. de Gendt, D. H. van Dorp, *ECS J. Solid State Sci. Technol.* **2020**, *9*, 084002.
[43] S. F. Bent, *Chemical Bonding at Surfaces and Interfaces*, Elsevier, Amsterdam, Netherlands, **2008**, pp. 323–395.
[44] S. v. d. Walt, S. C. Colbert, G. Varoquaux, *Comput. Sci. Eng.* **2011**, *13*, 22.
[45] T. E. Oliphant, *Comput. Sci. Eng.* **2007**, *9*, 10.
[46] G. Bradski, *Dobb's Journal: Software Tools for the Professional Programmer* **2000**, *25*, 120.
[47] F. de la Peña, T. Ostasevicius, V. T. Fauske, P. Burdet, P. Jokubauskas, M. Nord, E. Prestat, M. Sarahan, K. E. MacArthur, D. N. Johnstone, J. Taillon, J. Caron, T. Furnival, A. Eljarrat, S. Mazzucco, V. Migunov, T. Aarholt, M. Walls, F. Winkler, H.-W. Chang, hyperspy/hyperspy: HyperSpy 1.3 (v1.3). Zenodo **2017**, https://doi.org/10.5281/zenodo.583693.
[48] J. D. Hunter, *Comput. Sci. Eng.* **2007**, *9*, 90.